Effects of internal target structures on laser-driven neutron production

Yihang Zhang[1,3], Win-Min Wang[1,4,6*], Yutong Li[1,3,7*], Zhe Zhang[1], Paul McKenna[2], David Neely[2,5] and Jie Zhang[1,4,8]

[1] Beijing National Laboratory for Condensed Matter Physics, Institute of Physics, Chinese Academy of Sciences, Beijing 100190, China
[2] Department of Physics, Scottish Universities Physics Alliance (SUPA), University of Strathclyde, Glasgow, G4 0NG, UK
[3] School of Physical Sciences, University of Chinese Academy of Sciences, Beijing 100049, China
[4] Collaborative Innovation Center of IFSA (CICIFSA), Shanghai Jiao Tong University, Shanghai 200240, China
[5] Central Laser Facility, Science and Technology Facilities Council (STFC) Rutherford Appleton Laboratory (RAL), Didcot, OX11 0QX, UK
[6] Department of Physics, Renmin University of China, Beijing 100872, China
[7] Songshan Lake Materials Laboratory, Dongguan, Guangdong 523808, China
[8] Key Laboratory for Laser Plasmas (Ministry of Education) and School of Physics and Astronomy, Shanghai Jiao Tong University, Shanghai 200240, China

E-mail: `weiminwang1@126.com, ytli@iphy.ac.cn`

Abstract. We study neutron production in interactions of an intense laser pulse with solid, near-critical density and foam targets, by two-dimensional particle-in-cell simulations. We find that compared with solid and near-critical density targets, the neutron production from foam targets is more efficient because ion acceleration and ion-ion collisions are significantly enhanced. This is caused due to formation of ambipolar electrostatic fields among the multi-lamellas in the foam. The energy conversion efficiency from the laser pulse to the ions inside the foam target is up to 11%, 12-fold higher than the one achieved with a solid target for the same laser parameters. We also find that a foam target with thinner lamellas and larger pores between the lamellas is more favorable for neutron production due to higher laser energy absorption and longer distance for ion acceleration. The number of the neutrons can reach 10^7 from a foam target with a thickness of only 20 μm driven by a 10^{20} W/cm^2 laser pulse.

Keywords: neutron sources, ion acceleration, foam targets, laser-plasma interactions

1. Introduction

Neutron sources have been widely applied in material testing for fusion power plants [1], high temporal and spatial resolution radiography [2–4], neutron therapy [5] and neutron resonance spectroscopy [6]. Interactions of ultra-intense laser pulses with plasma can produce compact neutron sources with short duration in sub-ps or ps range [7] and

high-brightness [8, 9]. Therefore, theses novel neutron sources have attracted broad interest and been investigated both theoretically [10–12] and experimentally [13–15]. Photonuclear (γ, n) [16–18] and ion-acceleration-induced nuclear reactions [6, 9] are two ways to produce neutrons using intense, short laser pulses. In laser induced photonuclear reactions, hot electrons generate γ-rays through bremsstrahlung radiations in a high Z material converter, and then neutrons are produced via photonuclear reactions in the converter. For ion-acceleration-induced reactions, the prerequisite for efficient neutron production is the generation of large numbers of energetic ion collisions [14]. Different target structures including single solid bulk [14, 19], "pitcher-catcher" (P-C) [9, 20–22], cluster [23] targets have been investigated.

For a solid target irradiated by an intense laser pulse, the longitudinal ponderomotive force of the pulse induces an electrostatic field that accelerates the ions from the front surface [24]. Simultaneously, the ions at the rear surface of the target are also accelerated by the target normal sheath acceleration (TNSA mechanism) [25, 26]. However, only the forward-directed ions originating from the front surface contribute to the nuclear reactions through their collisions with the background cold nuclei inside the target [11, 27]. Compared with the TNSA at the rear surface, the ions accelerated at the front surface has lower energy and efficiency. Furthermore, there is almost no further acceleration of these ions inside the cold target bulk [28] due to the large cold electron return currents [29, 30].

To increase neutron yields, a pitcher-catcher (P-C) double target has been adopted and demonstrated [8, 9]. In this scheme, the first target is used to generate energetic ions and the ions enter and collide with the second target, which can efficiently produce neutrons via ion-ion collisions. It was reported in Ref. [9] that 10^{11} neutrons were achieved through D-D reactions when a pulse of 80 J and 10^{20} - 10^{21} W/cm^2 was used [9]. In recent years, progress on improvement and control of ion beam qualities [31–35] could further enable efficient neutron production. However the size of the neutron source in a P-C scheme is at the level of millimeter [36], much larger than the equivalent source in a single target [14], provided the same laser spot size is taken. This makes the neutron source less bright. Besides, ion acceleration from the first target is significantly suppressed by proton acceleration at the target rear due to contaminants, which is difficult to avoid [20, 21].

Cluster targets have also been used for neutron production [23]. When a laser pulse interacts with a cluster target, the absorbing efficiency of laser energy can approach 90% [37], and ions can be accelerated inside the whole target volume. For clusters with radius smaller than the quivering amplitude of a free electron $\xi = \frac{a_0 \lambda_0}{2\pi}$, where a_0 is the normalized laser electric field amplitude and λ_0 is the wavelength, most of the extracted electrons do not come back to the cluster [38]. The main acceleration mechanism is Coulomb explosion of the ion clouds, and the maximum ion energy is typically hundreds keV/nucleon [37]. For larger-sized cluster targets, the energy of the ions accelerated by stochastic electron heating can be several MeV [38].

Recently much attention has been paid to improving ion acceleration with a near-

critical density (NCD) target [39–44]. A laser pulse can penetrate deeper into such a target due to relativistically induced transparency and strong self-focusing can also occur [39]. Furthermore, the lower target density enhances the inhibition of fast electron propagation, so that more laser energy can be transferred to ions via these electrons [29, 43]. Protons close to 100 MeV has been demonstrated in a thin foil expanding to near-critical density [34] and about 200 MeV protons can be generated from a $2n_c$ target with a laser intensity of 3×10^{21} W/cm^2 [44]. High laser energy coupled to ions indicates an NCD target can be a candidate to enhance neutron production.

In this paper, we study effects of the internal structures of targets on neutron production. We perform two-dimensional (2D) particle-in-cell (PIC) simulations with the KLAPS code [45] and a Monte Carlo (MC) code to look at the neutron production with three types of targets, solid, NCD and foam targets. The ion acceleration and the angular, energy, temporal and spatial distributions of the neutrons produced in the targets are compared. The simulation results show that the efficient ion acceleration inside the whole bulk of a foam target can significantly enhance neutron production. The energy conversion efficiency from the laser pulse to ions accelerated inside the foam volume can reach 11.4%, 12 times higher than the one achieved with a solid target (0.9%) for equivalent laser parameters. The total number of neutrons as well as the number density of forward neutrons (in the laser direction) are increased by 2 orders of magnitude. The neutron number reaches 10^7 in a foam target with a thickness of 20 μm, when a 3×10^{20} W/cm^2, 44 fs laser pulse is used. Larger micro-pores and thinner lamellas of the foam target are more favorable for neutron production due to more efficient ion-ion collisions.

2. Simulation setup

2.1. Particle-in-Cell simulations

We use the 2D version of the KLAPS code to study ion acceleration in pure deuterium targets with different internal structures. In our simulations, a laser pulse propagates in the $+x$ direction with a wavelength of 1 μm and p-polarization along the y direction. The pulse is normally incident on a target located from $x = 22$ μm. The laser focal spot radius (electric field waist radius) R_0 is 9 μm and the pulse duration τ_0 is 44 fs in full width at half maximum (FWHM). The laser electric field is a normal Gaussian pulse, which is written by

$$\mathbf{E}(r,x') = \hat{r}a_0\frac{R_0}{R(x')}\exp(\frac{-r^2}{R^2(x')}) \exp[-\mathrm{i}kx' - \mathrm{i}k\frac{r^2}{2x'[1+(\frac{\pi{\omega_0}^2}{\lambda_0 x'})^2]} + \mathrm{i}\phi(x')], \quad (1)$$

r is the radial distance from the center axis of the beam and $x' = x - ct$. In our 2D simulations, we take the laser intensity value calculated in the 3D geometry. The peak intensity is 3.4×10^{20} W/cm^2, corresponding to the amplitude $a_0 = 5$ normalized by

$m_e c\omega_0/e$. The simulation box size is 100 μm × 50 μm with a spatial resolution of 0.025 μm both in the longitudinal (x) and transverse (y) directions. 64 simulation electrons and deuterons are adopted per cell.

We use three types of targets, solid, NCD and foam ones. To allow for effects of the prepulse of an intense laser pulse, a preplasma is included in the front of the targets with a density profile linearly increasing from $0.1n_c$ at $x = 22$ μm to $1n_c$ at $x = 30$ μm. In the main target area, for consistency, we keep the same average areal densities, for the three targets. The densities of the solid and NCD targets are set to be $10n_c$, located within 30 μm $\leqslant x \leqslant$ 34 μm, and $2n_c$, located within 30 μm $\leqslant x \leqslant$ 50 μm, respectively. To imitate the micro-structures in a foam target, which is consist of multi-micro-pores distributed irregularly, a simple model of regularly distributed lamellas (located in 30 μm $\leqslant x \leqslant$ 50 μm) is adopted, which is shown in Fig. 1. The thickness of the lamellas d is 0.1 μm with a density of $10n_c$, and the size of the micro-pores $L^2 = 1$ μm × 1 μm. These parameters are taken according to typical foam materials [46, 47]. The density of $10n_c$ is lower than a real solid material to reduce computational expense, nevertheless it involves the similar physical process of ion acceleration and electron dynamics as a real solid density.

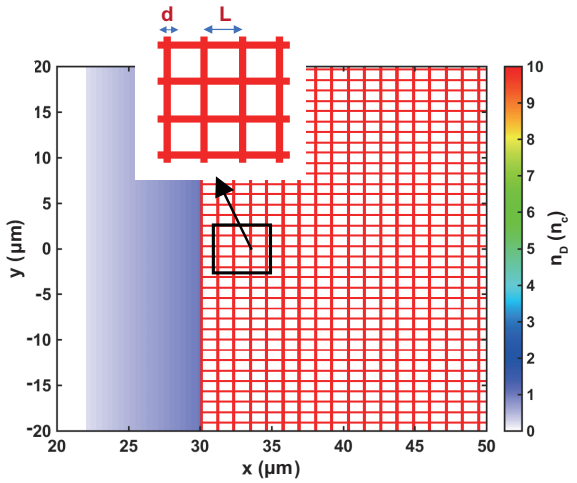

Figure 1. 2D initial density profile of the foam target. The inset illustrates inner structure parameters d and L, representing the lamella thickness and micro-pore size, respectively.

2.2. Monte Carlo post-processor for neutron production

In D-D reactions (D + D → ^{3}He +n), the volumetric reaction rate, that is, the number of reactions per unit time and per unit volume, is given by

$$R_{12} = n_1 n_2/(1 + \delta_{12})\sigma v \tag{2}$$

where n_1 and n_2 are number densities of two reacting deuteron macro-particles, σ is the cross section, and $v = |\mathbf{v_1} - \mathbf{v_2}|$ is their relative velocity. δ_{12} is the Kronecker symbol

(with $\delta_{12} = 1$, if the two reacting nuclei are the same, and $\delta_{12} = 0$ otherwise) [48]. The total cross section σ is equivalent to the integration of the differential cross section $d\sigma(\theta)/d\Omega$ over the solid angle, $\sigma = \int \frac{\mathrm{d}\sigma(\theta)}{\mathrm{d}\Omega}\mathrm{d}\Omega$. In principle, the differential cross section peaks on the deuteron colliding direction and has positive correlation with colliding energy E_r (related to relative velocity v) at any neutron emission angle θ_n (referred to the deuteron colliding direction). Neutron energy can be given by

$$E_n = \frac{M_D M_n}{(M_n + M_{He})^2} E_r (\sqrt{\eta + cos^2\theta_n} + cos\theta_n)^2, \tag{3}$$

where

$$\eta = \frac{M_n + M_{He}}{M_D M_n}(M_{He} - M_D + M_{He}\frac{Q}{E_r}), \tag{4}$$

and $Q = 3.266$ MeV is the reaction energy [49].

A Monte Carlo (MC) post-processor is developed to simulate the neutron production. From the PIC simulation, we randomly choose 10% of the deuterons and transfer the data of their positions, momenta and densities to the MC code. (The 10% sample is taken to reduce computational expense, while guaranteeing identical neutron energy and angular distributions.) This data transfer is performed with a time interval of 0.01 ps in the first 1.2 ps and 0.03 ps after 1.2 ps. Then, the evolution of the deuteron positions, momenta and densities obtained in the PIC simulation is included in the MC code. In the MC calculation, a deuteron pair is randomly chosen from the deuterons in the same PIC cell to calculate their collision energy and reaction rate with the relative velocity v of the given deuteron pair. With v, the differential cross sections $\mathrm{d}\sigma(\theta)/\mathrm{d}\Omega$ and total cross section σ can be found in the tabulated data through the cubic spline interpolation. By using (2)-(4), not only the neutron numbers and energies, but also their spatial, temporal and angular distributions can be calculated, with a spatial resolution of 0.025 μm, the same with the PIC simulation. To estimate realistic neutron number from a 2D planar simulation, usually one can assume the laser spot size as the z-direction size of the produced neutron beam. Here we adopt a more reasonable method in which we take the y-direction size of the accelerated deuteron beam as the z-direction size of the neutron source.

In our case the annihilation of reacting deuterons can be neglected. In an extreme situation with the maximum cross section of 0.1 barn and a deuteron with the light speed c colliding with a $10n_c$ plasma, one can deduce according to (2) that the maximum reaction probability is only 7.6×10^{-5}, much less than 1, in our whole simulation time.

3. Results

3.1. Neutron production

Figures 2 (a) and (b) show the temporal evolution of the neutron production rates P (in the unit of s^{-1}) and the spatial distributions of the volumetric production rates R (in the unit of $\mathrm{cm}^{-3}\mathrm{s}^{-1}$) along x-axis at 0.4 ps, respectively, where R is calculated

from (2) and P is the spatial integral of R over the whole targets. In the foam target, nuclear reactions occur inside the whole foam bulk [Fig. 2(b)] and R is as high as 5×10^{25} $\mathrm{cm^{-3}s^{-1}}$. The high R value maintains for a long time and therefore P keeps at a high level of 10^{17} $\mathrm{s^{-1}}$ from 0.1 ps to 1.2 ps as shown in Fig. 2(a). In both the solid and NCD targets, R and P have much lower levels and the nuclear reactions last shorter [Fig. 2(a)] within a smaller space [Fig. 2(b)]. Therefore, the total number of neutrons produced from the foam target is 4.4×10^{5}, much higher than the ones as 7.6×10^{3} and 2.3×10^{4} from the solid and NCD targets according to our PIC and MC simulations.

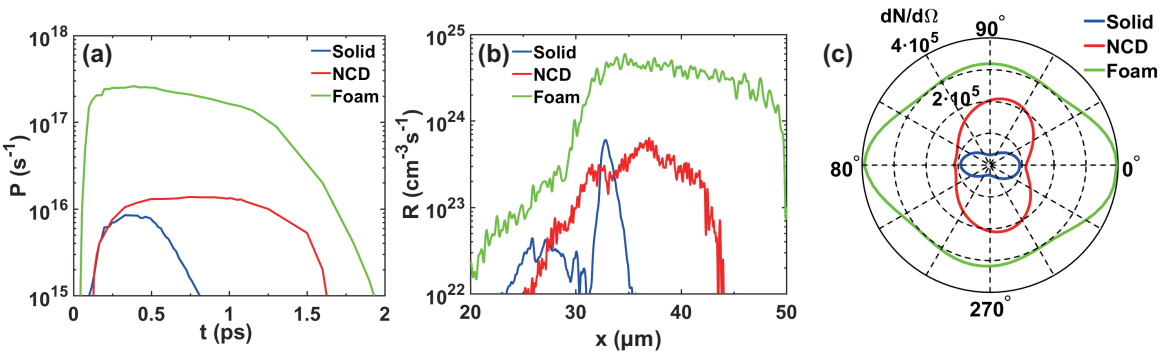

Figure 2. (a) Temporal evolution of the neutron production rates P; (b) longitudinal distributions of the volumetric neutron production rates R, which is calculated by formula (2) at 0.4 ps and averaged in y-direction; (c) neutron angular distributions ($\mathrm{d}N/\mathrm{d}\Omega$ in $\mathrm{MeV^{-1}}$) for the solid, NCD and foam targets. The data of neutron angular distributions from the solid and NCD targets are multiplied by 10.

Figure 2 (c) shows the neutron angular distributions. 0° is the laser propagating axis (also target normal). To show it clearly, the data of the solid and NCD targets are multiplied by 10. Neutrons from the solid target is anisotropic and mainly emitted in forward and backward directions. In the NCD target, the neutron emission appears a radial distribution. For the foam target, the neutron angular distribution is quasi-isotropic but stronger around 0° and 180°. Although the neutron beam has less directivity than the solid target, the number density in the laser direction is 40 times higher.

Figure 3 shows spectra of the neutrons emitted in 0° and 90° from the solid, NCD and foam targets. According to Eqs.(3) and (4), when the emission angle is in 140° -180°, the neutron energy is around 2 MeV. As shown in Fig. 3(a) and 3(b), in 0° of the solid target [blue curve in Fig. 3(a)] and 90° of the NCD target [red curve in Fig. 3(b)], neutron spectra have peaks around 2 MeV. This indicates deuteron backward acceleration in the solid target and radial transportation in the NCD target (which is symmetrical about x-axis). For deuteron collisions with energy below 1 MeV, neutron emission energy is around 2.5 MeV in 90° -120°. The neutron spectrum in 90° from the solid target has a peak around 2.5 MeV [blue curve in Fig. 3(b)]. One can expect that the collisions mainly happen along x-axis. In the case of the foam target, peaks around 2 and 2.5 MeV can be observed in both directions. Similar spectra in 0° and

199 90° indicate quasi-isotropic acceleration [green curves in Figs. 3(a) and (b)]. Also, when
200 the deuteron spectrum and angular distribution get broader, the neutron spectrum has
201 a slower break down at high energy, rather than a sharp cutoff. Figure 3 suggests that
there is much higher deuteron energy in the foam target.

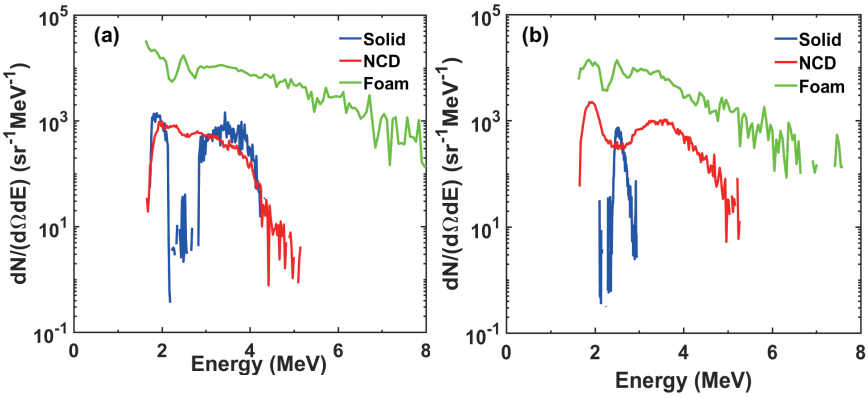

Figure 3. Spectra of the neutrons emitted at (a) 0° and (b) 90° from the solid, NCD and foam targets.

202

203 *3.2. Deuteron acceleration*

204 To further understand the neutron production presented above, we investigate the
205 electron dynamics and deuteron acceleration in the targets. Figures 4 (a)-(c) show
206 the laser electric fields and the electron densities n_e in different targets at $t = 0.1$ ps.
207 Figures 4 (d)-(f) show the longitudinal electrostatic field E_x and the deuteron densities
208 n_D at typical time of $t = 0.07$ ps for the solid target and $t = 0.13$ ps for the NCD and
209 foam targets, respectively, when the highest E_x appears. In the solid target, the laser
210 propagates to the dense surface of the plasma, and is reflected there [see Fig. 4(a)].
211 Numerous hot electrons move forward and escape from the target rear, then a strong
212 sheath electrostatic field is established [Fig. 4(d)]. This electrostatic field accelerates
213 deuterons forward through the TNSA mechanism at the rear surface [25]. Due to large
214 cold electron return currents, there is almost no electrostatic field induced inside the
215 solid target.

216 In the NCD target with $2n_c$, the laser pulse is able to propagate into the deep target
217 bulk and piles up the electrons, which is shown in the solid green line in Fig. 4(b). This is
218 caused by self-induced relativistic transparency [50] in low density plasma, which is also
219 controlled by momentum anisotropy and average energy of electrons [51]. There are also
220 corrugated bubbles generated due to the laser filamentation [52–54]. As the self-focusing
221 effect occurs, the maximum pulse intensity inside the target at $t = 0.1$ ps is increased to
222 8.5×10^{19} W/cm^2. As a result, the NCD target absorbs much more energy from the laser
223 pulse [52]. Whatsmore, the transport of hot electrons is more inhibited due to the low
224 background electron density [43], and this part of energy can be transferred to deuterons.
225 However, there is still no effective electrostatic field excited for deuteron acceleration

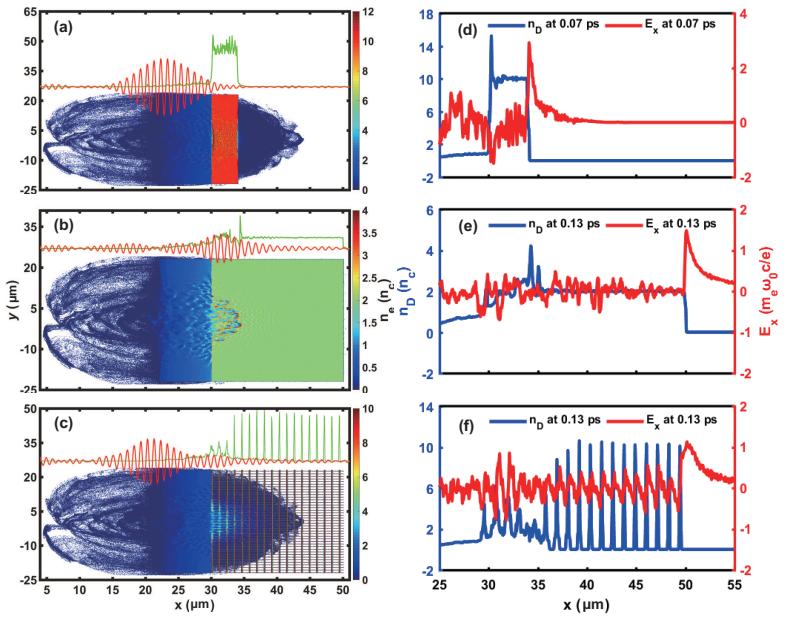

Figure 4. 2D snapshots of the electron densities n_e at $t = 0.1$ ps in the (a) solid, (b) NCD and (c) foam targets. The longitudinal distributions of the laser electric fields and electron densities at $y = 0$ are shown with the red and green lines, respectively. Electrostatic fields E_x (red lines) and deuteron densities n_D (blues lines) in the (d) solid, (e) NCD and (f) foam targets, respectively.

inside the target, as shown in Fig. 4(e), since the density distribution is continuous and some cold electron return currents can neutralize the field. The deuteron acceleration mainly happens at the front and rear side, like the solid target.

The foam target is analogous to a multi-layered solid target. Figure 4(c) shows that the first three plasma layers are exploded and become transparent at $t = 0.1$ ps, hence, the target also absorbs much laser energy. Beyond the layers reached by the laser pulse, hot electrons continue to move forward and penetrate further into the target bulk. Therefore, the background electrons in the following lamellas are heated up and expand into the micro-pores, forming ambipolar electrostatic fields among the lamellas, as shown in the red line in Fig. 4(f). Each ambipolar field will induce cascaded TNSA-like acceleration in two opposite local normal directions.

Figure 5 shows angular distribution of deuteron collision energy, where 0° represents the laser incident direction. In the solid target, deuterons with relatively high energies, which contribute to D-D collision inside target, are mainly generated near the target front surface. Forward-directed ions collide with cold nuclei in background plasma and backward ions with the preplasma [shown in Fig. 5(a)]. As a result, the neutron angular distribution is anisotropy [see Fig. 2(c)]. In the NCD target, the laser pulse can penetrate deeper and bores a hole inside the target as discussed before and the radial laser pondermotive force expels electrons transversely. The deuterons are pulled by electrons radially [Fig. 5(b)]. Therefore, the neutron emission appears a radial

distribution [Fig. 2(c)]. With the foam target, the ambipolar electrostatic fields among the lamellas [Fig. 4(f)] accelerate deuterons both forwards and backwards [Fig. 5(c) and 8(b)]. However, transverse deuteron acceleration mainly happens within a transverse size as the laser focal spot. This can explain the neutron angular distribution is quasi-isotropic but stronger around 0° and 180°, as shown in Fig. 2(c). For the solid and NCD targets, backward accelerated deuterons are less energetic than those from the foam. Since the background nuclei are under-dense in the region of preplasma (x < 30 μm), there are less nuclear reactions happening [see Fig. 2(b)]. In the foam target, however, due to the bulk acceleration by ambipolar electrostatic fields, energetic backward deuterons can cause higher reaction rates in the preplasma [Fig. 2(b)].

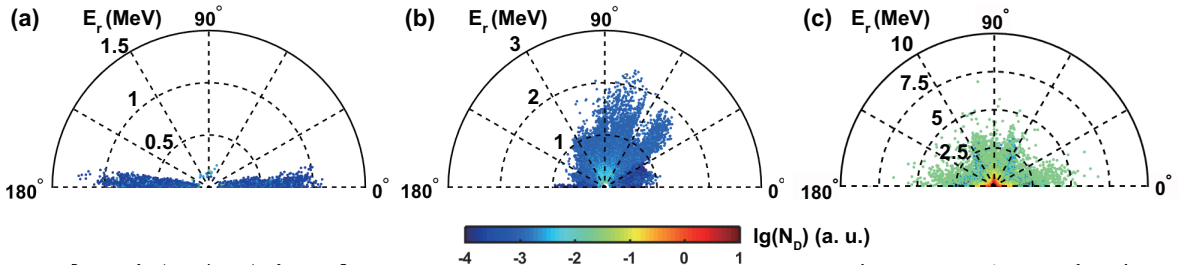

Figure 5. Angular distributions of deuteron colliding energy, where the solid, NCD and foam targets are shown in (a), (b) and (c), respectively.

The spectra of the deuterons inside the targets which contribute to the neutron production are shown in Fig. 6(a). The highest number of deuterons are generated in the foam target with cutoff energy around 4 MeV at around 0.33 ps. The maximum collision energy is 8 MeV as shown in Fig. 5(c), which is obtained when the colliding deuteron pairs have opposite velocities. Those collisions have higher reactivity σv for D-D reactions. Fig. 6(b) shows that the energy conversion efficiency from the laser pulse to the deuterons is the highest, up to 11.4%, inside the foam target. The efficiencies are only 2.7% and 0.9% inside the NCD and solid targets, respectively.

3.3. Optimization of laser and foam target parameters

In the above sections, we have taken a foam target with d = 0.1 μm, L = 1 μm and a total thickness of 20 μm s shown in Fig. 1 (we call it as "Foam1"), irradiated by a 3.3×10^{19} W/cm^2 laser pulse with a duration of 44 fs. When the duration is increased to 450 fs, the foam is heated to a relatively uniform plasma with a density around $2n_c$ at the pulse end. Generally, if the pulse is too long, the bulk acceleration by ambipolar electrostatic fields could be broken down, and the neutron production inside the target would be less efficient. In the following simulations we keep the laser duration of 44 fs and focal spot radius 9 μm unchanged and change the laser energy or intensity within from 1.7×10^{19} W/cm^2 to 3.0×10^{20} W/cm^2.

We also take other two foam targets with the lamella and micro-pore sizes changed. We take the Foam2 with d = 1 μm, L = 1 μm (thicker lamella) and Foam3 with d = 0.1

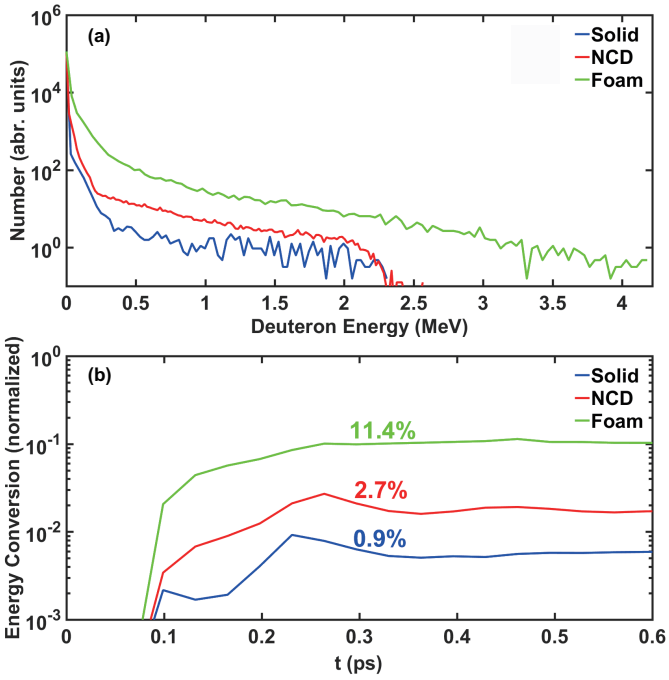

Figure 6. (a) Energy spectra of the deuterons inside the targets at $t = 0.33$ ps for different targets. (b) Energy conversion efficiencies from the laser to deuterons inside the targets as a function of time.

μm, $L = 1.5$ μm (larger micro-pore), according to real foam materials [46, 47] and our computation resource. When d or L changed, the density integrals along both x-axis and y-axis are kept the same. It is shown in Fig. 7 that when larger micro-pores are adopted (Foam3), the neutron number increases with the growing laser intensity much more rapidly and the neutron production is more efficient compared with the standard Foam1. However, the neutron production becomes inefficient within a large range of the laser intensity when Foam2 with thicker lamellas is taken. These results suggest that larger pores and thinner lamella is more favorable for nuclear reactions.

Figures 8(a) and (c) show there is high density accumulation in between the lamellas in Foam2 with thicker lamellas and shorter void spaces, and Figs. 8(b) and (d) indicate deuteron colliding energy gets higher in Foam3 with thinner lamellas and larger void spaces. For Foam3, a longer acceleration distance of deuterons can be obtained for cascaded TNSA-like acceleration around each lamella. In addition, thinner lamellas in Foam3 can increase laser energy absorption, which is more favorable to deuteron acceleration. The deuteron energy enhancement causes higher neutron production according to Eq.(2).

We summarize our simulation results on different laser and target parameters in Table 1. The anisotropy of the neutrons is estimated by the number ratio of 0° and 90° ($N_{0°}/N_{90°}$). When the laser intensity is increased to 3.0×10^{20} W/cm^2, deuterons inside Foam3 have 15% of the laser energy, and can be accelerated to 20 MeV. The total neutron number can be up to 1.1×10^7 within 2.5 ps. In this case, the volumetric

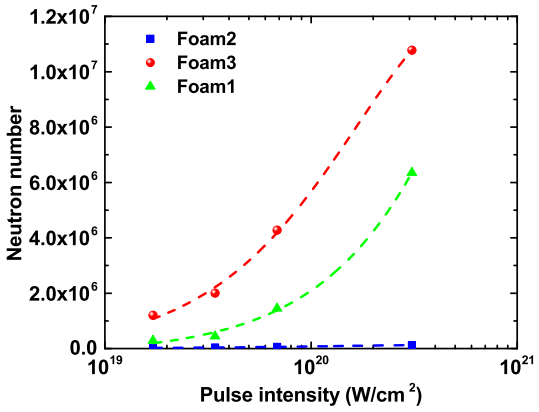

Figure 7. Neutron numbers as functions of the laser intensities in 3 kinds of foam targets

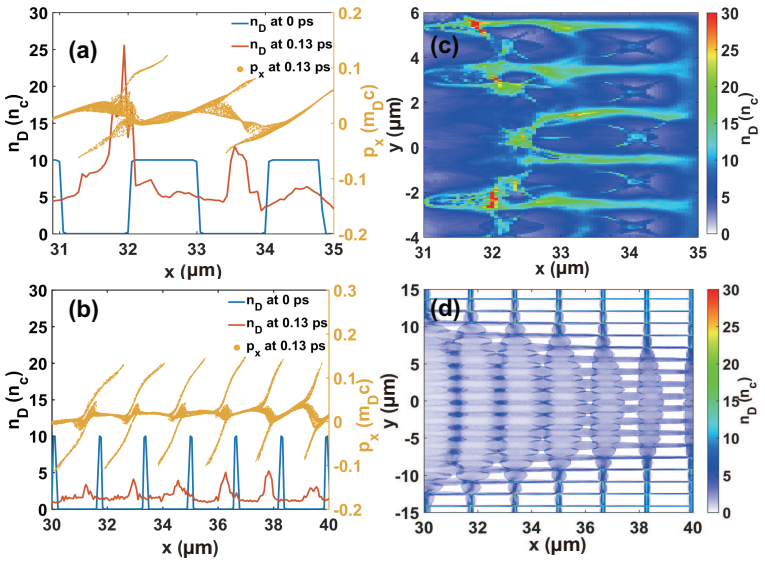

Figure 8. (a) and (b) are the longitudinal phase space (yellow points) and densities (blue and red lines for 0 and 0.13 ps) of deuterons in Foam2 and Foam3, where the laser intensity is taken as 3.0×10^{20} W/cm^2. (c) and (d) are 2D deuteron densities of Foam2 and Foam3 at $t = 0.13$ ps, where one can see deuteron expansion, accumulation and collision inside the void spaces of foam targets.

reaction rate exceeds 3×10^{28} cm^{-3}s^{-1}, and the reaction rate reaches 8×10^{18} s^{-1}, much higher than the ones in traditional methods for neutron source production [55, 56]. Note that we have taken foam targets with thicknesses of micrometer levels in our simulations to reduce the computing expense. One can expected that if a thick (millimeters) target is taken in a real experiment [27], the neutron number can be significantly enhanced since a smaller part of energy flux flows out from the target to the right vacuum.

Table 1. Data related to neutron sources in different targets and laser parameters.

Target	I_L(W/cm^2)	d(μm)	L(μm)	$\frac{E_D}{E_L}$(%)[a]	$\frac{\mathrm{d}N}{\mathrm{d}\Omega}(0°)(\mathrm{sr}^{-1})$	$\frac{\mathrm{d}N}{\mathrm{d}\Omega}(90°)(\mathrm{sr}^{-1})$	$\mathrm{d}N_{0°}/\mathrm{d}N_{90°}$[b]	Neutron yield
Solid	3.4×10^{19}	n.a.	n.a.	0.9	9.7×10^{2}	4.0×10^{2}	2.4	7.6×10^{3}
NCD	3.4×10^{19}	n.a.	n.a.	2.7	1.2×10^{3}	2.0×10^{3}	0.6	2.3×10^{4}
Foam1	3.4×10^{19}	0.1	1	11	4.0×10^{4}	3.3×10^{4}	1.2	4.4×10^{5}
Foam1	3.0×10^{20}	0.1	1	12	4.7×10^{5}	5.9×10^{5}	0.8	6.4×10^{6}
Foam2	3.4×10^{19}	1	1	3.0	3.0×10^{3}	3.3×10^{3}	0.9	3.8×10^{4}
Foam2	3.0×10^{20}	1	1	4.4	1.1×10^{4}	9.6×10^{3}	1.2	1.2×10^{5}
Foam3	3.4×10^{19}	0.1	1.5	13	1.9×10^{5}	1.5×10^{5}	1.3	2.0×10^{6}
Foam3	3.0×10^{20}	0.1	1.5	15	8.2×10^{5}	9.1×10^{5}	0.9	1.1×10^{7}

[a] $\frac{E_D}{E_L}$ is the energy conversion rate from the laser pulse to deuterons inside the target.
[b] $\mathrm{d}N_{0°}/\mathrm{d}N_{90°}$ is the anisotropy of the neutron source represented by the ratio of neutron number per steradian at 0° and 90°.

4. Conclusions

We have investigated neutron production based on the laser-driven deuteron acceleration in the solid, NCD and foam targets with the same areal density. Our 2D PIC simulations have shown that the deuteron acceleration has the highest efficiency inside the foam target than the other two, due to efficient bulk acceleration. Consequently, much stronger deuteron-deuteron collisions result in much more neutrons with higher energy produced. The neutron number is 60 times higher than the one with the solid target.

We have optimized parameters of the foam target and the laser pulse. A target with larger pores between the lamellas and thinner lamellas is more favorable to produce neutrons due to a longer distance of ion acceleration and higher efficiency of laser energy absorption. The total neutron number can be up to 10^7 with only a 20-μm-thick foam target irradiated by a 3×10^{20} W/cm^2 laser pulse. This work provides a method to produce high-flux short-duration neutron sources, which could find applications in fast neutron radiography and neutron scattering for material studies [2, 56, 57].

Acknowledgments

This work is supported by the Science Challenge Project (No.TZ2016005), the National Key R&D Program of China (Grant No.2018YFA0404801), the National Nature Science Foundation of China (Grants No.11520101003, 11827807, 11775302, 11861121001 and 11535001), the Strategic Priority Research Program of the Chinese Academy of Sciences (Grant No.XDB16010200 and XDB07030300) and the Newton foundation.

References

[1] Perkins L J, Logan B G, Rosen M D, Perry M D, de la Rubia T D, Ghoniem N M, Ditmire T, Springer P T and Wilks S C 2000 *Nuclear Fusion* **40** 1

[2] Loveman R, Bendahan J, Gozani T and Stevenson J 1995 *Nuclear Instruments and Methods in Physics Research Section B: Beam Interactions with Materials and Atoms* **99** 765–768

[3] Anderson I S, McGreevy R L and Bilheux H Z 2009 *Neutron Imaging and Applications* (Springer Science+Business Media) pp 210–211

[4] Arikawa Y, Matsubara S, Abe Y, Kato Y, Kishimoto H, Yogo A, Nishimura H, Nakai M, Shiraga H, Fujioka S, Azechi H, Otake Y, Mima K and Honda Y 2017 *Selected Papers from the 31st International Congress on High-Speed Imaging and Photonics* **10328** 103280T

[5] Gray L H and Read J 1943 *Nature* **152** 53

[6] Higginson D P, McNaney J M, Swift D C, Bartal T, Hey D S, Kodama R, Le Pape S, Mackinnon A, Mariscal D, Nakamura H, Nakanii N, Tanaka K A and Beg F N 2010 *Physics of Plasmas* **17** 100701

[7] Macchi A 2006 *Applied Physics B* **82** 337–340

[8] Kar S, Green A, Ahmed H, Alejo A, Robinson A P L, Cerchez M, Clarke R, Doria D, Dorkings S, Fernandez J, Mirfayzi S R, McKenna P, Naughton K, Neely D, Norreys P, Peth C, Powell H, Ruiz J A, Swain J, Willi O and Borghesi M 2016 *New Journal of Physics* **18** 053002

[9] Roth M, Jung D, Falk K, Guler N, Deppert O, Devlin M, Favalli A, Fernandez J, Gautier D, Geissel M, Haight R, Hamilton C E, Hegelich B M, Johnson R P, Merrill F, Schaumann G, Schoenberg K, Schollmeier M, Shimada T, Taddeucci T, Tybo J L, Wagner F, Wender S A, Wilde C H and Wurden G A 2013 *Physical Review Letters* **110** 044802

[10] Hu L X, Yu T P, Shao F Q, Zhu Q J, Yin Y and Ma Y Y 2015 *Physics of Plasmas* **22** 123104

[11] Toupin C, Lefebvre E and Bonnaud G 2001 *Physics of Plasmas* **8** 1011–1021

[12] Ellison C L and Fuchs J 2010 *Physics of Plasmas* **17** 113105

[13] Torrisi L 2014 *Molecules* **19** 17052–17065

[14] Pretzler G, Saemann A, Pukhov A, Rudolph D, Schätz T, Schramm U, Thirolf P, Habs D, Eidmann K, Tsakiris G D, Meyer-ter Vehn J and Witte K J 1998 *Physical Review E* **58** 1165

[15] Abe Y, Sunahara A, Lee S, Yanagawa T, Zhang Z, Arikawa Y, Morace A, Nagai T, Ikenouchi T, Tosaki S, Kojima S, Sakata S, Satoh N, Watari T, Nishihara K, Kawashima T, Yogo A, Sakagami H, Shiraga H, Nishimura H, Mima K, Azechi H, Norimatsu T, Nakai M and Fujioka S 2017 *Applied Physics Letters* **111** 233506

[16] Ledingham K W, Spencer I I, McCanny T, Singhal R P, Santala M I, Clark E, Watts I I, Beg F N, Zepf M, Krushelnick K, Tatarakis M, Dangor A E, Norreys P A, Allott R, Neely D, Clark R J, Machacek A C, Wark J S, Cresswell A J, Sanderson D C and Magill J 2000 *Physical Review Letters* **84** 899–902

[17] Pomerantz I, McCary E, Meadows A R, Arefiev A, Bernstein A C, Chester C, Cortez J, Donovan M E, Dyer G, Gaul E W, Hamilton D, Kuk D, Lestrade A C, Wang C, Ditmire T and Hegelich B M 2014 *Physical Review Letters* **113** 184801

[18] Jiao X J, Shaw J M, Wang T, Wang X M, Tsai H, Poth P, Pomerantz I, Labun L A, Toncian T, Downer M C and Hegelich B M 2017 *Matter and Radiation at Extremes* **2** 296–302

[19] Disdier L, Garconnet J P, Malka G and Miquel J L 1999 *Physical Review Letters* **82** 1454

[20] Maksimchuk A, Raymond A, Yu F, Petrov G M, Dollar F, Willingale L, Zulick C, Davis J and Krushelnick K 2013 *Applied Physics Letters* **102** 191117

[21] Alejo A, Krygier A G, Ahmed H, Morrison J T, Clarke R J, Fuchs J, Green A, Green J S, Jung D, Kleinschmidt A, Najmudin Z, Nakamura H, Norreys P, Notley M, Oliver M, Roth M, Vassura L, Zepf M, Borghesi M, Freeman R R and Kar S 2017 *Plasma Physics and Controlled Fusion* **59** 064004

[22] Mirfayzi S R, Alejo A, Ahmed H, Raspino D, Ansell S, Wilson L A, Armstrong C, Butler N M H, Clarke R J, Higginson A, Kelleher J, Murphy C D, Notley M, Rusby D R, Schooneveld E,

Borghesi M, McKenna P, Rhodes N J, Neely D, Brenner C M and Kar S 2017 *Applied Physics Letters* **111** 044101
[23] Ditmire T, Zweiback J, Yanovsky V P, Cowan T E, Hays G and Wharton K B 1999 *Nature* **398** 489
[24] Maksimchuk A, Gu S, Flippo K, Umstadter D and Bychenkov V Y 2000 *Physical Review Letters* **84** 4108
[25] Wilks S C, Langdon A B, Cowan T E, Roth M, Singh M, Hatchett S, Key M H, Pennington D, MacKinnon A and Snavely R A 2001 *Physics of Plasmas* **8** 542–549
[26] Zepf M, Clark E L, Krushelnick K, Beg F N, Escoda C, Dangor A E, Santala M I K, Tatarakis M, Watts I F, Norreys P A, Clarke R J, Davies J R, Sinclair M A, Edwards R D, Goldsack T J, Spencer I and Ledingham K W D 2001 *Physics of Plasmas* **8** 2323–2330
[27] Willingale L, Petrov G M, Maksimchuk A, Davis J, Freeman R R, Joglekar A S, Matsuoka T, Murphy C D, Ovchinnikov V M, Thomas A G R, Van Woerkom L and Krushelnick K 2011 *Physics of Plasmas* **18** 083106
[28] Li Y T, Sheng Z M, Ma Y Y, Jin Z, Zhang J, Chen Z L, Kodama R, Matsuoka T, Tampo M, Tanaka K A, Tsutsumi T, Yabuuchi T, Du K, Zhang H Q, Zhang L and Tang Y J 2005 *Physical Review E* **72** 066404
[29] Batani D, Antonicci A, Pisani F, Hall T A, Scott D, Amiranoff F, Koenig M, Gremillet L, Baton S, Martinolli E, Rousseaux C and Nazarov W 2002 *Physical Review E* **65** 066409
[30] Bell A R, Davies J R, Guerin S and Ruhl H 1997 *Plasma Physics and Controlled Fusion* **39** 653
[31] Arefiev A, Toncian T and Fiksel G 2016 *New Journal of Physics* **18** 105011
[32] Wagner F, Deppert O, Brabetz C, Fiala P, Kleinschmidt A, Poth P, Schanz V A, Tebartz A, Zielbauer B, Roth M, Stohlker T and Bagnoud V 2016 *Physical Review Letters* **116** 205002
[33] Kar S, Ahmed H, Prasad R, Cerchez M, Brauckmann S, Aurand B, Cantono G, Hadjisolomou P, Lewis C L, Macchi A, Nersisyan G, Robinson A P, Schroer A M, Swantusch M, Zepf M, Willi O and Borghesi M 2016 *Nature Communications* **7** 10792
[34] Higginson A, Gray R J, King M, Dance R J, Williamson S D R, Butler N M H, Wilson R, Capdessus R, Armstrong C, Green J S, Hawkes S J, Martin P, Wei W Q, Mirfayzi S R, Yuan X H, Kar S, Borghesi M, Clarke R J, Neely D and McKenna P 2018 *Nature Communications* **9** 724
[35] Scott G G, Carroll D C, Astbury S, Clarke R J, Hernandez-Gomez C, King M, Alejo A, Arteaga I Y, Dance R J, Higginson A, Hook S, Liao G, Liu H, Mirfayzi S R, Rusby D R, Selwood M P, Spindloe C, Tolley M K, Wagner F, Zemaityte E, Borghesi M, Kar S, Li Y, Roth M, McKenna P and Neely D 2018 *Physical Review Letters* **120** 204801
[36] Alejo A, Green A, Ahmed H, Robinson A P L, Cerchez M, Clarke R, Doria D, Dorkings S, Fernandez J, McKenna P, Mirfayzi S R, Naughton K, Neely D, Norreys P, Peth C, Powell H, Ruiz J A, Swain J, Willi O, Borghesi M and Kar S 2016 *Nuclear Instruments and Methods in Physics Research Section A: Accelerators, Spectrometers, Detectors and Associated Equipment* **829** 176–180
[37] Esirkepov T, Bingham R, Bulanov S, Honda T, Nishihara K and Pegoraro F 2000 *Laser and Particle Beams* **18** 503–506
[38] Breizman B N, Arefiev A V and Fomyts'kyi M V 2005 *Physics of Plasmas* **12** 056706
[39] Bulanov S S, Bychenkov V Y, Chvykov V, Kalinchenko G, Litzenberg D W, Matsuoka T, Thomas A G, Willingale L, Yanovsky V, Krushelnick K and Maksimchuk A 2010 *Physics of Plasmas* **17** 043105
[40] Willingale L, Nilson P M, Thomas A G R, Bulanov S S, Maksimchuk A, Nazarov W, Sangster T C, Stoeckl C and Krushelnick K 2011 *Physics of Plasmas* **18** 056706
[41] Bin J H, Ma W J, Wang H Y, Streeter M J, Kreuzer C, Kiefer D, Yeung M, Cousens S, Foster P S, Dromey B, Yan X Q, Ramis R, Meyer-ter Vehn J, Zepf M and Schreiber J 2015 *Physical Review Letters* **115** 064801
[42] Willingale L, Nagel S R, Thomas A G, Bellei C, Clarke R J, Dangor A E, Heathcote R, Kaluza M C, Kamperidis C, Kneip S, Krushelnick K, Lopes N, Mangles S P, Nazarov W, Nilson P M

and Najmudin Z 2009 *Physical Review Letters* **102** 125002
[43] Bond D J, Hares J D and Kilkenny J D 1980 *Physical Review Letters* **45** 252
[44] Nakamura T, Bulanov S V, Esirkepov T Z and Kando M 2010 *Physical Review Letters* **105** 135002
[45] Wang W M, Gibbon P, Sheng Z M and Li Y T 2015 *Physical Review E* **91** 013101
[46] Okihara S, Esirkepov T, Nagai K, Shimizu S, Sato F, Hashida M, Iida T, Nishihara K, Norimatsu T, Izawa Y and Sakabe S 2004 *Physical Review E* **69** 026401
[47] Franke D and Pahl M H 1997 *Chemical Engineering and Processing: Process Intensification* **36** 175–183
[48] Atzeni S and Meyer-ter Vehn J 2004 *The Physics of Inertial Fusion: BeamPlasma Interaction, Hydrodynamics, Hot Dense Matter* (Oxford University Press on Demand) pp 3–4
[49] Youssef A, Kodama R, Habara H, Tanaka K A, Sentoku Y, Tampo M and Toyama Y 2005 *Physics of Plasmas* **12** 110703
[50] Palaniyappan S, Hegelich B M, Wu H C, Jung D, Gautier D C, Yin L, Albright B J, Johnson R P, Shimada T, Letzring S, Offermann D T, Ren J, Huang C, Hörlein R, Dromey B, Fernandez J C and Shah R C 2012 *Nature Physics* **8** 763–769
[51] Stark D J, Bhattacharjee C, Arefiev A V, Toncian T, Hazeltine R D and Mahajan S M 2015 *Physical Review Letters* **115** 025002
[52] Wilks S C, Kruer W L, Tabak M and Langdon A B 1992 *Physical Review Letters* **69** 1383
[53] Ma Y Y, Chang W W, Yan Y, Cao L H and Yue Z W 2001 *Chinese Physics Letters* **18** 1628–1631
[54] Ma Y, Zhao J, Li Y, Li D, Chen L, Liu J, Dann S J D, Ma Y, Yang X, Ge Z, Sheng Z and Zhang J 2018 *Proceedings of the National Academy of Sciences of the United States of America* **115** 6980–6985
[55] Mank G, Bauer G and Mulhauser F 2011 *Reviews of Accelerator Science & Technology* **04** 219–233
[56] Anderson I S, Andreani C, Carpenter J M, Festa G, Gorini G, Loong C K and Senesi R 2016 *Physics Reports* **654** 1–58
[57] Faenov A, Matsubayashi M, Pikuz T, Fukuda Y, Kando M, Yasuda R, Iikura H, Nojima T, Sakai T, Shiozawa M, Kodama R and Kato Y 2015 *High Power Laser Science and Engineering* **3** e27